

Article

Up-Conversion Luminescence and Magnetic Properties of Multifunctional Er³⁺/Yb³⁺-Doped SiO₂-GdF₃/LiGdF₄ Glass Ceramics

Corina Secu ¹, Cristina Bartha ² , Cristian Radu ^{1,2} and Mihail Secu ^{1,*}¹ National Institute of Materials Physics, Atomistilor 405A, 077125 Magurele, Romania² Faculty of Physics, University of Bucharest, Atomistilor 405, 077125 Magurele, Romania

* Correspondence: msecu@infim.ro

Abstract: Glassy nanocomposites containing Yb³⁺/Er³⁺-doped GdF₃ and LiGdF₄ nanocrystals have been prepared by controlled crystallization of the xerogel and the structural, up-conversion luminescence, and magnetic properties were analyzed and discussed. Structural and morphological analysis showed uniform distribution of both GdF₃ and LiGdF₄ nanocrystals (tens of nm size), embedded in silica glass matrix as the result of thermal decomposition of the trifluoroacetates, revealed as a strong exothermic peak at about 300 °C; the Li-ions co-doping showed a strong influence on the GdF₃ and LiGdF₄ nanocrystalline fraction. The energy dispersive spectrometry mapping showed Gd, F and Yb, Er within the nanocrystals but not in the silica glass matrix. X-ray diffraction pattern analysis indicated the crystalline lattice distortion consistent with the Yb/Er incorporation in both fluoride nanocrystals. The “green” (²H_{11/2}, ⁴S_{3/2}) → ⁴I_{15/2}) and “red” (⁴F_{9/2} → ⁴I_{15/2}) up-conversion luminescences at 525, 545, and 660 nm observed under 980 nm laser light pumping were assigned to the Er³⁺ ions deexcitation through a two-photon process. The magnetic properties of the nanocomposite are strongly temperature dependent. The magnetization hysteresis loops show a ferromagnetic behavior at low temperatures (5K) related to the rare-earth ions contribution and the saturation magnetization of 39 emu/g. At 300 K a paramagnetic behavior was observed that was ascribed to the non-interacting localized nature of the magnetic moment of the rare-earth ions. Hence, such novel, multifunctional magnetic and optical materials can allow the intertwining between magnetism and photonics and might offer new opportunities for new magneto-optical device development.

Keywords: glass ceramic; fluorides; sol–gel; nanocrystals; up-conversion luminescence; magnetism



Citation: Secu, C.; Bartha, C.; Radu, C.; Secu, M. Up-Conversion Luminescence and Magnetic Properties of Multifunctional Er³⁺/Yb³⁺-Doped SiO₂-GdF₃/LiGdF₄ Glass Ceramics. *Magnetochemistry* **2023**, *9*, 11. <https://doi.org/10.3390/magnetochemistry9010011>

Academic Editor: Jiang Li

Received: 30 November 2022

Revised: 22 December 2022

Accepted: 26 December 2022

Published: 29 December 2022



Copyright: © 2022 by the authors. Licensee MDPI, Basel, Switzerland. This article is an open access article distributed under the terms and conditions of the Creative Commons Attribution (CC BY) license (<https://creativecommons.org/licenses/by/4.0/>).

1. Introduction

The pursuit of technological miniaturization in our modern knowledge-based society places a strong focus on discovering novel materials with multifunctional properties such as magnetic, optical, and electrical ones. Among them, oxyfluoride nano-glass ceramics with rare-earth (RE)-doped fluoride nanocrystals precipitated in a silica glass matrix are key materials for a wide variety of optical and photonic applications due to their outstanding optical properties: high transparency due to the nanocrystal's smallness (i.e., 10 to 20 nm size) and remarkable luminescence properties related to the crystalline environment of the rare-earth ions ([1] and references therein). A suitable, controllable, and flexible method for their preparation is provided by the sol–gel chemistry with its advantages: good control of fluorine nanocrystalline phase precipitation and RE-dopant contents as well as lower processing temperature ([2,3] and references therein).

Among the RE ions, gadolinium (III) presents a special interest because of its dual luminescent and paramagnetic properties which are of great interest for a wide range of applications such as multifunctional imaging, and simultaneous diagnosis and therapy [4]. The overlapping between the 4f energy levels, ⁶P_J states of Gd³⁺, and UV-excited states of RE-ions promotes an efficient energy transfer between them [5–8] and efficient

quantum cutting phenomena have been observed in Eu^{3+} -doped LiGdF_4 , GdF_3 [7,8]. On the other hand, the paramagnetic response of the Gd^{3+} ions to the externally applied magnetic field is related to the seven unpaired inner 4f electrons which are closely bound to the nucleus and effectively shielded by the outer closed shell electrons $5s^25p^6$ from the crystal field [9]. Hence, a great deal of research efforts was paid to the investigation and analysis of optical and magnetical properties of Gd^{3+} -doped fluoride nanomaterials $\text{GdF}_3:\text{Eu}^{3+}$ [9], KGdF_4 [10], $\text{NaYb}_{1-x}\text{Gd}_x\text{F}_4$ [11], and $\text{LiY}(\text{Gd})\text{F}_4:\text{Yb}/\text{Er}$ [12]. However, previous investigations of sol-gel-derived glass ceramics with GdF_3 nanocrystals embedded in the glass matrix are limited to the analysis of luminescence properties of the co-dopant RE-ions [13–15], and the magnetic properties have been overlooked/missed. Crystalline phases analysis of RE^{3+} -doped $\text{SiO}_2\text{-GdF}_3$ oxyfluoride glass ceramics has shown the precipitation of both hexagonal and orthorhombic GdF_3 nanocrystals [16,17] or only orthorhombic one [13–15] in the silica matrix, depending on the synthesis path. The photoluminescence and decay profiles studies indicate the distribution of optically active ions into the silicate environment and low-vibrational GdF_3 crystal lattice [17] and the occurrence of the $\text{Gd}^{3+}/\text{RE}^{3+}$ (RE = Tb, Eu) energy transfer [14,15].

Within the present study, we successfully synthesized bi-phase glassy nanocomposites containing $\text{Yb}^{3+}/\text{Er}^{3+}$ -doped GdF_3 and LiGdF_4 nanocrystals by using controlled crystallization of the xerogel. We investigated the influence of Li-co-doping ions on the structural composition, up-conversion luminescence, and magnetic properties of the glassy nanocomposite.

2. Materials and Methods

2.1. Samples Preparation

For the preparation of the xerogel Er^{3+} (1%)/ Yb^{3+} (4%)-doped $90\text{SiO}_2\text{-5LiGdF}_4$ (mol%) xerogels, we have used the sol-gel synthesis route as described in ref. [18,19] and reagent grade of tetraethylorthosilicate (TEOS), trifluoroacetic acid (TFA), ethyl alcohol, acetic acid, and deionized water as starting materials (all from Alfa-Aesar, Heysham, Lancashire, UK). In the first step, TEOS was hydrolyzed under constant stirring with a mixed solution of ethanol and water and using glacial acetic acid as a catalyst; the molar ratio was 1:4:3.5:0.5. A second solution of $\text{Er}(\text{CH}_3\text{COO})_3$, $\text{Yb}(\text{CH}_3\text{COO})_3$, $\text{Li}(\text{CH}_3\text{COO})$, $\text{Gd}(\text{CH}_3\text{COO})_3$ and TFA with the molar ratio for Er:Yb:Li:Gd:F of 1:4:5:5:122 was prepared, mixed, and added to the first solution. After an additional vigorous stirring for 1 h at room temperature, the mixed solution was aged at room temperature for a week in a sealed Petri dish. Then, the wet-gel obtained was dried up to $120\text{ }^\circ\text{C}$ for 1 week to form the xerogel. Glass-ceramic sample (denoted as 1LiGC) was obtained after subsequent thermal treatments in air at $530\text{ }^\circ\text{C}$ for 60 min. By using a similar procedure, we have prepared nano-glass ceramics samples without Li-co-doping and with Li-ions excess, i.e., by using 2:1 and 4:1 for the Li to Gd molar ratio; corresponding glass-ceramic samples are denoted as 0LiGC, 2LiGC, and 4LiGC.

2.2. Samples Characterization

Differential scanning calorimetry (DSC) analysis has been performed by using a differential scanning calorimeter 204 F1 Phoenix (NETZSCH-Gerätebau GmbH, Selb, Germany) and the powder samples (9 mg mass) were encapsulated in aluminum crucibles. The measurements were performed from room temperature up to $590\text{ }^\circ\text{C}$, in a flux of synthetic air (80% N_2 /20% O_2) with a heat flow of 20 mW/min and a heating rate of $10\text{ }^\circ\text{C}/\text{min}$. The accuracy of the heat flow measurements was $\pm 0.001\text{ mW}$ and the temperature precision was $\pm 0.01\text{ }^\circ\text{C}$. For the structural characterization of the materials by X-ray diffractometry (XRD), we used a BRUKER D8 ADVANCE type X-ray diffractometer (Billerica, MA, USA), in focusing geometry, equipped with a copper target X-ray tube and LynxEye one-dimensional detector, in the 15 to 55° range with 0.05° step and 2 s integration time. The analysis of the XRD pattern was performed by using the Powercell dedicated software [20]. For the transmission electron microscopy (TEM) analysis of the sample, we used a JEM-ARM200F (JEOL, Tokyo, Japan) transmission electron microscope operating at 200 kV electron beam

accelerating voltage and equipped with energy-dispersive X-ray spectrometer (EDS). The magnetic properties characterization was performed using an MMPS SQUID magnetometer from Quantum Design (San Diego, CA, USA). The hysteresis loops were acquired at two different temperatures (5 K and 300 K) under an applied magnetic field between -4 T and 4 T. The evolution of magnetization in the field-cooled (FC) and zero field-cooled (ZFC) regime as a function of temperature was made under an applied magnetic field of 300 Oe. The up-conversion (UC) luminescence spectra were recorded at room temperature by using a FluoroMax 4P spectrophotometer (HORIBA Jobin Yvon, Kyoto, Japan) and a laser light module (200 mW) centered at 980 nm.

3. Results and Discussion

3.1. Thermal Analysis

Differential scanning calorimetry (DSC) curves recorded on $\text{Yb}^{3+}/\text{Er}^{3+}$ -doped $\text{SiO}_2\text{-GdF}_3(\times 2\text{Li mol.}\%)$ xerogel samples (Figure 1) revealed the evolution of the structural evolution of the xerogel during the thermal decomposition.

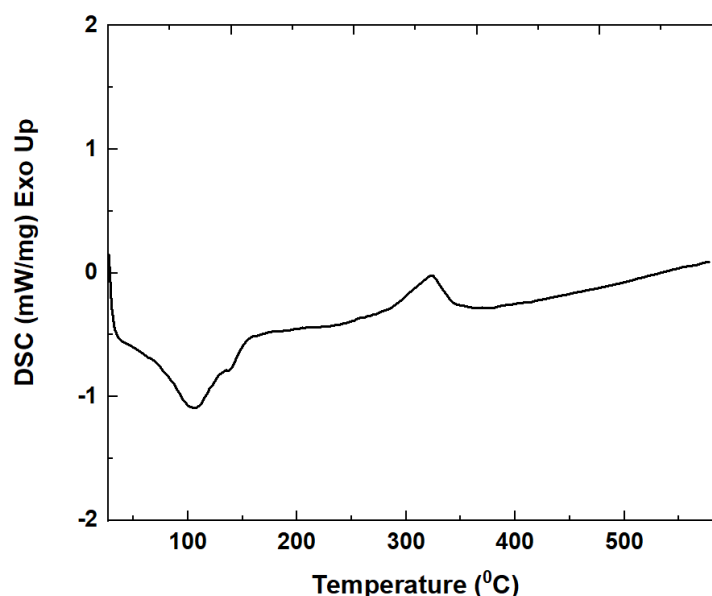


Figure 1. Differential scanning calorimetry (DSC) curves recorded on $\text{Yb}^{3+}/\text{Er}^{3+}$ -doped $\text{SiO}_2\text{-GdF}_3(\times 2\text{Li mol.}\%)$ xerogel sample.

The DSC curve recorded on $\text{Yb}^{3+}/\text{Er}^{3+}$ -doped $\text{SiO}_2\text{-GdF}_3(\times 2\text{Li mol.}\%)$ xerogel sample (Figure 1) shows an exothermic peak at about 100 °C with a small shoulder, due to the water evaporation and thermal decomposition of organic residues such as ethanol and acetic acid [21]. The 313 °C exothermic peak is close to 290 °C as shown by $\text{SiO}_2\text{-GdF}_3$ xerogel and it was assigned to the gadolinium trifluoroacetate $\text{Gd}(\text{CF}_3\text{COO})_3$ decomposition with subsequent GdF_3 nanocrystalline phase precipitation [17]. The small temperature shift is most probably due to the overlapping of the lithium and RE-trifluoroacetates decomposition processes [22].

3.2. Structural Analysis

The XRD patterns of the xerogel and the glass-ceramic samples are depicted in Figure 2. The initial xerogel shows a broad background consistent with the amorphous structure of the silica matrix (not shown). The pattern of undoped $\text{SiO}_2\text{-GdF}_3$ nano-glass ceramic is similar to the xerogel, it shows no diffraction peaks, but for the 0LiGC, 1LiGC, 2LiGC, and 4LiGC samples, we can recognize the extra-diffraction peaks assigned to the nanocrystalline phases precipitation in the glass matrix, GdF_3 (PDF 012-0788) and LiGdF_4 (PDF 060-0476) [23]. The XRD patterns of the Li-co-doped samples indicate a strong effect on

the structural properties of the glass ceramic samples revealed by the angle shift to higher angles and peaks ratio change. In addition, the nanocrystal growth process in the glassy matrix is strongly influenced by the ionic environment and ionic impurities [24]. For lower doping levels (up to 1%Li mol%), the XRD pattern shows the GdF_3 phase crystallization that gradually evolves to the LiGdF_4 phase crystallization for 4Li mol% doping level; both phases are observed for 2%Li mol% doping level. We have to mention that the Li^+ ions are quite small and therefore their actual concentration is likely to be much smaller because of the losses (such as diffusion, evaporation) during the glass ceramic thermal processing.

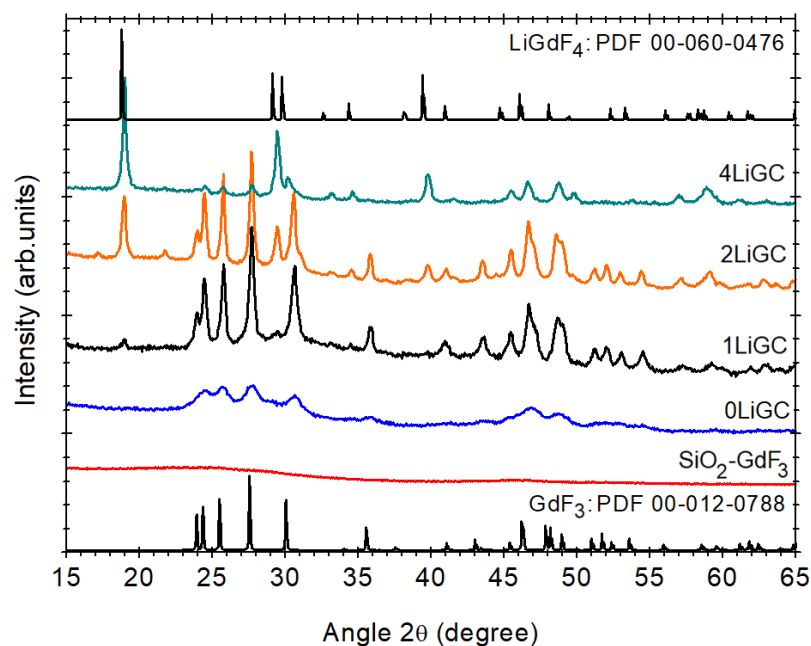


Figure 2. Normalized XRD patterns of $\text{SiO}_2\text{-GdF}_3$ and $\text{Yb}^{3+}/\text{Er}^{3+}$ -doped $\text{SiO}_2\text{-GdF}_3$ (x2Li mol.%) nano-glass ceramic with different Li-ions doping levels; the PDF files of GdF_3 and LiGdF_4 are included.

The results of the XRD patterns analysis of the glass-ceramic samples presented in Table 1 indicated differences in the lattice parameters compared to those from the ICDD database [23], consistent with distortions of the crystalline lattice. Despite the Gd-trifluoroacetate decomposition revealed by the thermal analysis curves, there is no evidence of the crystallization process after annealing of undoped $\text{SiO}_2\text{-GdF}_3$ xerogel. However, the Y,Er-ions doping initiates the crystallization of small GdF_3 nanocrystals of ≈ 10 nm size within the 0LiGC sample (Figure 2). It was shown that RE-doping has a great influence on the growth process, crystallographic phase, their size, and optical emission properties of the resulting nanocrystals [25]. For the selective synthesis of RE-doped LaF_3 and NaLaF_4 nanocrystals, the nanocrystal growth process has been used as a theoretical model based on the free energy approach [26]. Therefore, the formation of the GdF_3 nanocrystalline phase might be due to a decrease in the energetic barrier for the nanocrystal formation caused by lanthanide doping. The lattice parameters variation is consistent with a contraction of the cell volume of $\approx 1\%$ compared to the orth- GdF_3 (Table 1). As the ionic radius of 8-fold coordinated Yb^{3+} ions (105.3 pm) and Er^{3+} ions (100.4 pm) are much lower than that of 8-fold coordinated Gd^{3+} ions (119 pm) [27] the contraction effect is assigned to the Yb,Er ions incorporation within the GdF_3 nanocrystals.

Table 1. The results of the X-ray diffraction (XRD) pattern analysis of Yb³⁺/Er³⁺-doped SiO₂-GdF₃-LiGdF₄ nano-glass ceramic; the lattice parameters for GdF₃ (JCPDS-file 012-0788) and LiGdF₄ (JCPDS-file 060-0476) [13] are included for comparison.

Glass-Ceramic Sample/ Lattice Parameters	a (Å)	GdF ₃ b (Å)	c (Å)	Cell Volume (Å) ³	a (Å)	LiGdF ₄ c (Å)	Cell Volume (Å) ³
GdF ₃ (JCPDS 012-0788)	6.571	6.984	4.393	201.6			
0Li	6.476	6.973	4.402	198.8			
1Li	6.471	6.915	4.407	197.2			
2Li	6.471	6.905	4.395	196.4	5.171	10.878	290.8
4Li					5.174	10.878	289.0
LiGdF ₄ (JCPDS 060-0476)					5.219	10.971	298.8

For additional Li co-doped samples, the GdF₃ nanocrystals size increases to about 30 nm with a further decrease in the lattice parameters and the cell volume contraction too, up to $\cong 2.5\%$ for 2LiGC. Hence, besides the crystallinity improvement, Li-co-doping shows a high influence on the relative magnitude of the peaks; they are shifted to higher angles consistent with the crystalline lattice relaxation (contraction). As the difference between the ionic radii of Li⁺ and Gd³⁺ ions is relatively large, this makes Li⁺ ions enter easily into the substitutional position in the GdF₃ crystalline phase [28] accompanied by the contraction of the cell volume; fluorine vacancies and/or oxygen ions incorporated during the nanocrystals precipitation [29] may act as charge compensators. The precipitation of the LiGdF₄ nanocrystalline phase starts to develop and both phases are observed in the 2LiGC sample. The 4LiGC sample shows dominantly the LiGdF₄ nanocrystalline phase accompanied by a high contraction of $\cong 3\%$ of the lattice cell volume. A similar cell high distortion was observed in Yb/Er-doped Li(Gd,Y)F₄ nanoparticles: a = b = 5.177 Å and c = 10.773 Å and V = 288.7 Å³ was associated with a strong contraction of the lattice induced by the Yttrium(III) ions co-doping [30].

Further comments can be made about the crystallization mechanism of the Y/Er-doped SiO₂-GdF₃-LiGdF₄ nano-glass ceramic. According to the previous electron microscopy investigations, the crystallization processes of the alkali-earth fluorides within silica glass ceramics rely on the formation of small congeries particles composed of many, small nanocrystals (few nm) at low temperatures (400 °C) and proceed with their separation and homogenously distribution within the matrix for higher temperatures, above 500 °C [31,32]. However, in the present case, the glass ceramization is not a very simple process; the 2LiGC glass-ceramic sample shows the crystallization of only the GdF₃ nanocrystalline phase for temperature processing between 250 and 325 °C, and the LiGdF₄ nanocrystalline phase is observed only at higher temperature (Figure S1; Supplementary Material). Moreover, no obvious crystallization can be evidenced on SiO₂-GdF₃ xerogel samples processed for higher temperatures up to 700 °C. Therefore, the crystallization mechanism seems to be a more complex one and further investigations are necessary to reveal it.

3.3. Morphological Analysis

The electron microscopy images (Figure 3) show a large number of GdF₃ and LiGdF₄ nanoparticles embedded in the silica matrix with a spheric morphology (Figure S2; Supplementary Material) and the selected area electron diffraction (SAED) pattern (Figure 3) confirms the assignment.

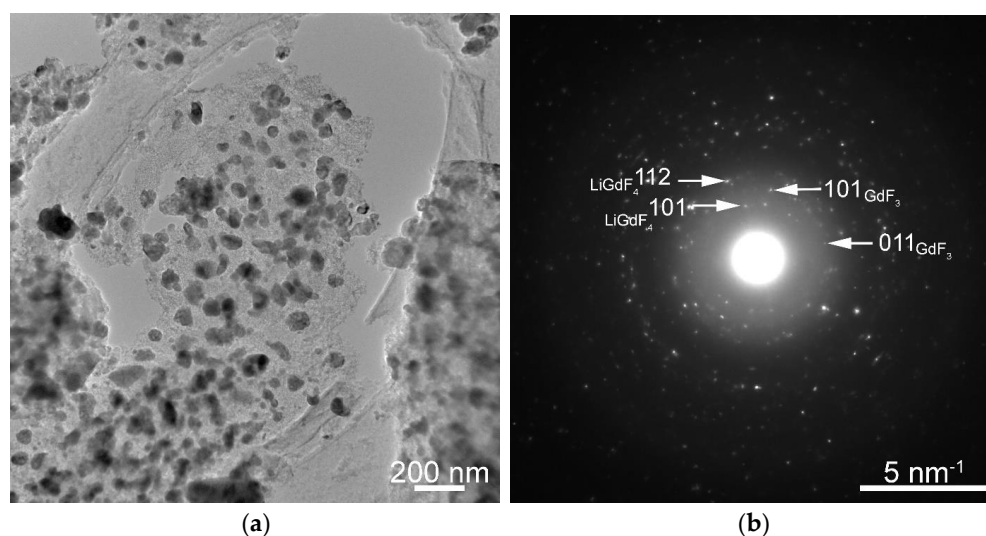


Figure 3. Low-magnification TEM images (a) and the corresponding SAED pattern (b) of the $\text{Yb}^{3+}/\text{Er}^{3+}$ -doped $\text{SiO}_2\text{-GdF}_3/\text{LiGdF}_4$ nano-glass ceramic (2LiGC).

The nanoparticles' size lies in the 50–100 nm range and the size distribution shows two maxima at around 20 nm and 60 nm (Figure S3; Supplementary Material). The EDX spectral analysis of the glass-ceramic sample (Figure S4; Supplementary Material) showed the presence of the elements from the precursor reagents: 32Si, 46O, 3Gd, 17F, and 2Yb (at%) in relatively good agreement with the precursors: 28Si, 56O, 2.5Li, 1.5Gd, 10.5F, 1Yb, and 0.5Er (at%). The EDS mapping images presented in Figure 4 show a uniform distribution of the Si and O and the localization of the Gd, F, Yb, and Er within the nanoparticles, as expected. The signal recorded on a single particle is too weak and noisy and therefore it is not possible to make a reliable quantitative measurement of the Gd/F atomic ratio in order to determine their respective phase— GdF_3 or LiGdF_4 .

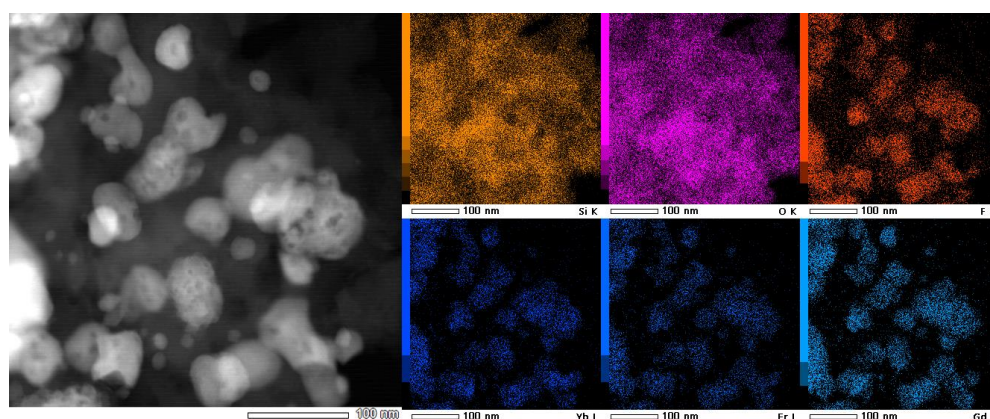


Figure 4. STEM images of the $\text{Yb}^{3+}/\text{Er}^{3+}$ -doped $\text{SiO}_2\text{-GdF}_3/\text{LiGdF}_4$ nano-glass ceramic (2LiGC) and the corresponding EDS mapping.

3.4. Up-Conversion Luminescence Properties

Figure 5 presents the up-conversion luminescence recorded on $\text{Yb}^{3+}/\text{Er}^{3+}$ -doped $\text{SiO}_2\text{-GdF}_3\text{-LiGdF}_4$ nano-glass ceramic with different Li-ions doping levels under 980nm laser light pumping. The spectra show the characteristic *green* (${}^2H_{11/2}, {}^4S_{3/2} \rightarrow {}^4I_{15/2}$) and *red* (${}^4F_{9/2} \rightarrow {}^4I_{15/2}$) luminescent emissions due to the Er^{3+} ions and their magnitude is strongly dependent on the Li-co-doping level.

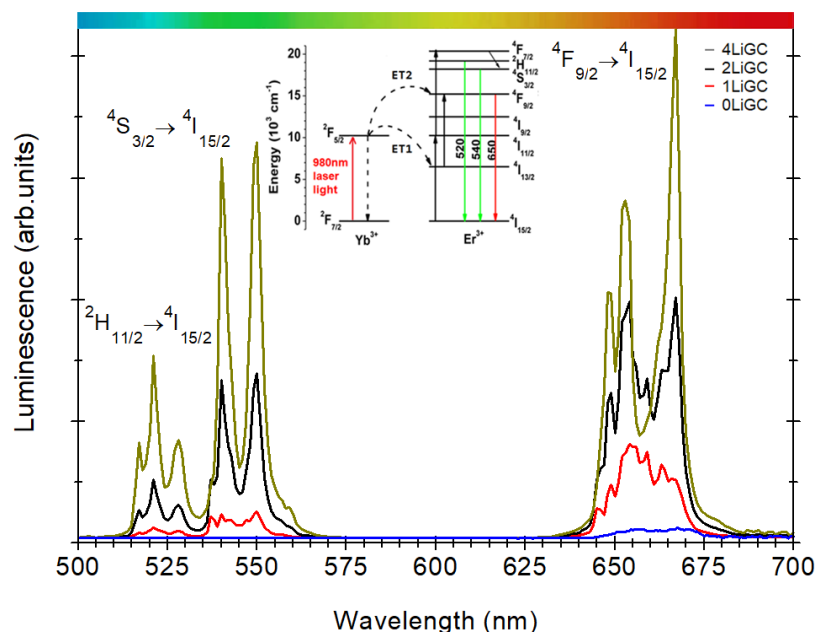


Figure 5. Up-conversion luminescence spectra recorded on Yb³⁺/Er³⁺-doped SiO₂-GdF₃/LiGdF₄ nano-glass ceramic with different Li-ions doping levels under 980 nm laser light pumping. The energy levels diagram of the Yb³⁺ and Er³⁺ ions and the main processes are shown in the inset.

The UC luminescence mechanism has been widely investigated in various Yb/Er-doped materials (nanocrystals, glasses, and glass ceramics) [33–35], and therefore, we do not address them in detail here. It is based on the efficient absorption of infrared light photons (around 1000 nm) by the Yb³⁺ ions (${}^2F_{7/2} \rightarrow {}^2F_{5/2}$ transition) followed by a two-step energy transfer process (ET) to neighboring Er³⁺ ions with the characteristic *green* and *red* luminescent emissions. The 980 nm laser light pumping promotes the population of the high energy ${}^4F_{7/2}$ levels through the ET1 and ET2 processes. The lower energy emitting levels (${}^2H_{11/2}$, ${}^4S_{3/2}$) and ${}^4F_{9/2}$ are then populated via multi-phonon and cross-relaxation (Yb³⁺–Er³⁺) processes, followed by the *green* ($({}^2H_{11/2}, {}^4S_{3/2}) \rightarrow {}^4I_{15/2}$) and *red* (${}^4F_{9/2} \rightarrow {}^4I_{15/2}$) luminescence emissions. For the undoped sample, the signal is hardly seen but Li-ions doping promoted a progressive enhancement of integral UC luminescence signal (Figure 5) and for the 4LiGC nano-glass ceramic sample it becomes comparable to that observed on Yb³⁺/Er³⁺-doped LiYF₄ nanocrystals [12]. The slight change in the peaks shape follows the nanocrystalline phase changes with the Li-doping level, from GdF₃ (for 1LiGC) to LiGdF₄ (for 4LiGC) (Figure 2).

3.5. Magnetic Properties

The magnetization hysteresis loops recorded at room temperature and low temperatures (5K) on Yb³⁺/Er³⁺-doped SiO₂-GdF₃/LiGdF₄ nano-glass ceramic (2LiGC) sample are depicted in Figure 6. The magnetization curves show a ferromagnetic behavior at low temperatures (5K) which is related to the sublattice coupling of the three rare-earth ions, Gd³⁺, Yb³⁺, and Er³⁺ present in the sample. A similar behavior was observed in GdF₃ [36] and Eu³⁺/Ce³⁺-doped GdF₃ [37] and assigned to the ferromagnetic interactions between ions. The saturation magnetization of 39 emu/g is smaller than for Eu³⁺/Ce³⁺-doped GdF₃ or NaGdF₄ [37] most probably to the nonmagnetic silica matrix. According to the molecular field theory [38], the interaction between magnetic moments of the rare earths is stronger at low temperatures and it rapidly decreases with the temperature increases. The total magnetic moment calculated at low temperature is 51.65 μ_B . This value is slightly increased compared to the theoretical magnetic moment of this type of material (40.8 μ_B) and is most likely due to a modified stoichiometry generated by the variation of oxygen in the structure that favors the appearance of distortions with an effect on the interaction between the spin

couplings. At room temperature, the saturation magnetization decreases, and a paramagnetic behavior was observed that was ascribed to the thermal fluctuation that changes the magnetic ordering of the rare-earth magnetic spins. The value of magnetic mass susceptibility 0.25×10^{-4} emu/g Oe is smaller than 0.94×10^{-4} emu/g Oe for Eu^{3+} -doped GdF_3 [9] or 0.53×10^{-4} emu/g Oe for $\text{Yb}^{3+}/\text{Er}^{3+}$ -doped GdF_3 [39] but higher than for RE-doped KGdF_4 of 1.64×10^{-5} emu/g Oe [10]. The field-cooled (FC) and zero field-cooled (ZFC) curves recorded on $\text{Yb}^{3+}/\text{Er}^{3+}$ -doped $\text{SiO}_2\text{-GdF}_3/\text{LiGdF}_4$ nano-glass ceramic (2LiGC) in a magnetic field of 300 Oe are depicted in Figure 7. They show an increase in the FC curve at low temperatures (below 125 K) assigned to the magnetic ordering temperature of the rare-earth sublattices.

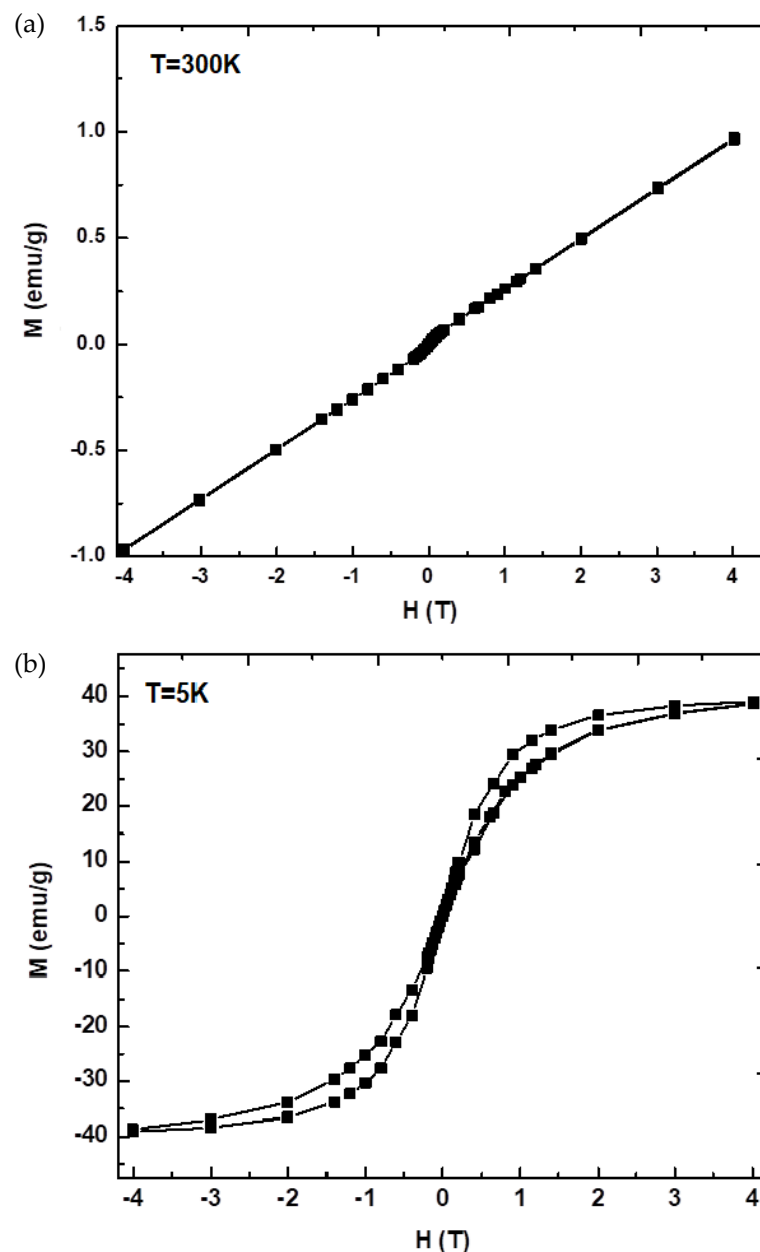


Figure 6. The magnetization hysteresis loops recorded at room temperature (a) and 5K (b) on $\text{Yb}^{3+}/\text{Er}^{3+}$ -doped $\text{SiO}_2\text{-GdF}_3/\text{LiGdF}_4$ nano-glass ceramic (2LiGC).

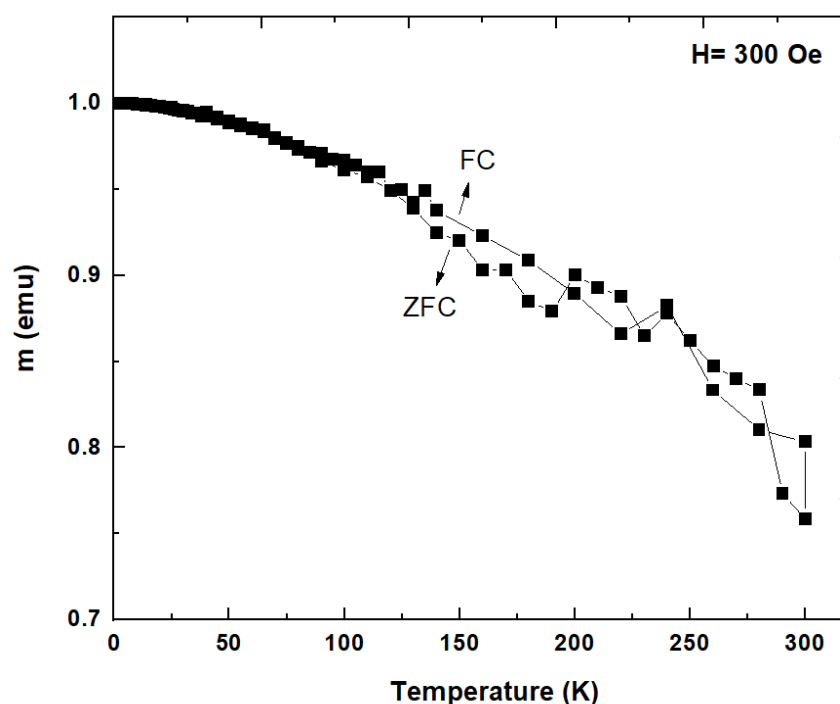


Figure 7. The temperature dependence of the magnetization in the field-cooled (FC) and zero field-cooled (ZFC) regime recorded on $\text{Yb}^{3+}/\text{Er}^{3+}$ -doped $\text{SiO}_2\text{-GdF}_3/\text{LiGdF}_4$ nano-glass ceramic (2LiGC) under 300 Oe applied magnetic field.

4. Conclusions

We have prepared glassy nanocomposites with $\text{Yb}^{3+}/\text{Er}^{3+}$ -doped GdF_3 and LiGdF_4 nanocrystals embedded by using the sol-gel method followed by controlled crystallization of the dried xerogel.

Thermal analysis has evidenced the decomposition of the trifluoroacetates at about 300 °C which is accompanied by the precipitation of both GdF_3 and LiGdF_4 nanocrystalline fraction only for Li co-doped samples. The crystalline lattice distortion is consistent with the Yb/Er incorporation in both fluoride nanocrystals.

Structural and morphological analysis of the $\text{Yb}^{3+}/\text{Er}^{3+}$ -doped $\text{SiO}_2\text{-GdF}_3/\text{LiGdF}_4$ nano-glass ceramic (2LiGC) showed uniform distribution of Yb/Er-doped GdF_3 and LiGdF_4 nanocrystals (tens of nm size), inside the silica glass matrix

Under 980 nm laser light pumping, the glass-ceramic samples show the characteristic Er^{3+} ions luminescence, “green” (${}^2\text{H}_{11/2}$, ${}^4\text{S}_{3/2}$ \rightarrow ${}^4\text{I}_{15/2}$) and “red” (${}^4\text{F}_{9/2}$ \rightarrow ${}^4\text{I}_{15/2}$) up-conversion luminescences at 525, 545, and 660 nm and follow the nanocrystalline phase changes with the Li-doping level. The up-conversion luminescence increases and it becomes comparable to other upconverter materials such as Yb,Er-doped LiYF_4 nanocrystals [12].

The $\text{Yb}^{3+}/\text{Er}^{3+}$ -doped $\text{SiO}_2\text{-GdF}_3/\text{LiGdF}_4$ nano-glass ceramic (2LiGC) shows a ferromagnetic behavior at low temperatures (5K) due to the ferromagnetic interactions between RE^{3+} ions. The value of saturation magnetization of 39 emu/g is smaller than for $\text{Eu}^{3+}/\text{Ce}^{3+}$ -doped GdF_3 or NaGdF_4 [37] most probably to the nonmagnetic silica matrix. At 300 K a paramagnetic behavior was observed that was ascribed to the non-interacting localized nature of the magnetic moment of the RE^{3+} ions.

Sol-gel processing assures a high crystallinity and is very well suited for the “spin-coating” deposition of thin film. By proper RE-ion doping and compositional tuning, new magnetic properties can be induced and added to the optical ones, paving the way for new magneto-optical devices.

Supplementary Materials: The following supporting information can be downloaded at: <https://www.mdpi.com/article/10.3390/magnetochemistry9010011/s1>.

Author Contributions: All the authors collaborated for the physical characterization and analysis of all the data: C.S. was involved in the sample preparation and XRD measurements; C.B. was responsible for the thermal analysis and magnetic measurements; M.S. was responsible for the optical properties (up-conversion luminescence) and structural analysis and C.R. was responsible for the morphological analysis by using transmission electron microscopy. All the authors contributed to discussions and reviewed the manuscript. All authors have read and agreed to the published version of the manuscript.

Funding: This research was funded by the Romanian Ministry of Research and Innovation (MCI) through the grant PN19-03 Core Program of NIMP (2020) and PN-III-P2-2.1-PED-2021-2007 (contract no. 676 PED/2022).

Institutional Review Board Statement: Not applicable.

Informed Consent Statement: Not applicable.

Data Availability Statement: Not applicable.

Conflicts of Interest: The authors declare no conflict of interest.

References

1. De Pablos-Martin, A.; Duran, A.; Pascual, M.J. Nanocrystallisation in oxyfluoride systems: Mechanisms of crystallization and photonic properties. *Int. Mater. Rev.* **2012**, *57*, 165–186. [\[CrossRef\]](#)
2. Gorni, G.; Velázquez, J.J.; Mosa, J.; Balda, R.; Fernández, J.; Durán, A.; Castro, Y. Transparent Glass-Ceramics Produced by Sol-Gel: A Suitable Alternative for Photonic Materials. *Materials* **2018**, *11*, 212. [\[CrossRef\]](#) [\[PubMed\]](#)
3. Secu, M.; Secu, C.; Bartha, C. Optical Properties of Transparent Rare-Earth Doped Sol-Gel Derived Nano-Glass Ceramics. *Materials* **2021**, *14*, 6871. [\[CrossRef\]](#) [\[PubMed\]](#)
4. Li, X.; Zhao, D.; Zhang, F. Multifunctional Upconversion-Magnetic Hybrid Nanostructured Materials: Synthesis and Bioapplications. *Theranostics* **2013**, *3*, 292–305. [\[CrossRef\]](#) [\[PubMed\]](#)
5. Guan, H.; Sheng, Y.; Xu, C.; Dai, Y.; Xie, X.; Zou, H. Energy transfer and tunable multicolor emission and paramagnetic properties of GdF₃:Dy³⁺, Tb³⁺, Eu³⁺ phosphors. *Phys. Chem. Chem. Phys.* **2016**, *18*, 19807–19819. [\[CrossRef\]](#) [\[PubMed\]](#)
6. Wang, W.Z.; Li, J.K.; Liu, Z.M. Controlling the morphology and size of (Gd_{0.98-x}Tb_{0.02}Eu_x)₂O₃ phosphors presenting tunable emission: Formation process and luminescent properties. *J. Mater. Sci.* **2018**, *53*, 12265–12283. [\[CrossRef\]](#)
7. Wegh, R.T.; Donker, H.; Oskam, K.D.; Meijerink, A. Visible quantum Eu³⁺ cutting in doped gadolinium fluorides via downconversion. *J. Lumin.* **1999**, *82*, 93–104. [\[CrossRef\]](#)
8. Wegh, R.T.; Donker, H.; Oskam, K.D.; Meijerink, A. Visible quantum cutting in LiGdF₄:Eu³⁺ through downconversion. *Science* **1999**, *283*, 663–666. [\[CrossRef\]](#)
9. Wong, H.T.; Chan, H.L.W.; Hao, J.H. Magnetic and luminescent properties of multifunctional GdF₃:Eu³⁺ nanoparticles. *Appl. Phys. Lett.* **2009**, *95*, 022512. [\[CrossRef\]](#)
10. Yang, L.W.; Zhang, Y.Y.; Li, J.J.; Li, Y.; Zhong, J.X.; Chu, P.K. Magnetic and upconverted luminescent properties of multifunctional lanthanide doped cubic KGdF₄ nanocrystals. *Nanoscale* **2010**, *2*, 2805–2810. [\[CrossRef\]](#)
11. Chen, D.Q.; Yu, Y.L.; Huang, F.; Yang, A.P.; Wang, Y.S. Lanthanide activator doped NaYb_{1-x}Gd_xF₄ nanocrystals with tunable down-, up-conversion luminescence and paramagnetic properties. *J. Mater. Chem.* **2011**, *21*, 6186–6192. [\[CrossRef\]](#)
12. Secu, C.E.; Bartha, C.; Matei, E.; Negri, C.; Crisan, A.; Secu, M. Gd³⁺ co-doping influence on the morphological, up-conversion luminescence and magnetic properties of LiYF₄:Yb³⁺/Er³⁺ nanocrystals. *J. Phys. Chem. Solids* **2019**, *130*, 236–241. [\[CrossRef\]](#)
13. Pawlik, N.; Szpikowska-Sroka, B.; Sołtys, M.; Pisarski, W.A. Optical properties of silica sol-gel materials singly- and doubly doped with Eu³⁺ and Gd³⁺ ions. *J. Rare Earths* **2016**, *34*, 786–795. [\[CrossRef\]](#)
14. Szpikowska-Sroka, B.; Pawlik, N.; Goryczka, T.; Pisarski, W.A. Influence of silicate sol-gel host matrices and catalyst agents on luminescence properties of Eu³⁺/Gd³⁺ under different excitation wavelengths. *RSC Adv.* **2015**, *5*, 98773–98782. [\[CrossRef\]](#)
15. Pawlik, N.; Szpikowska-Sroka, B.; Pietrasik, E.; Goryczka, T.; Pisarski, W.A. Photoluminescence and energy transfer in transparent glass-ceramics based on GdF₃:RE³⁺ (RE = Tb, Eu) nanocrystals. *J. Rare Earths* **2019**, *37*, 1137–1144. [\[CrossRef\]](#)
16. Fujihara, S.; Koji, S.; Kimura, T. Structure and Optical Properties of (Gd,Eu)F₃-Nanocrystallized Sol-Gel Silica Films. *J. Mater. Chem.* **2004**, *14*, 1331–1335. [\[CrossRef\]](#)
17. Velázquez, J.J.; Mosa, J.; Gorni, G.; Balda, R.; Fernández, J.; Pascual, L.; Durán, A.; Castro, Y. Transparent SiO₂-GdF₃ sol-gel nano-glass ceramics for optical applications. *J. Sol-Gel Sci. Technol.* **2019**, *89*, 322–332. [\[CrossRef\]](#)
18. Fujihara, S.; Mochizuki, C.; Kimura, T. Formation of LaF₃ microcrystals in sol-gel silica. *J. Non-Cryst. Solids* **1999**, *244*, 267. [\[CrossRef\]](#)

19. Secu, M.; Secu, C.E. Up-conversion luminescence of $\text{Er}^{3+}/\text{Yb}^{3+}$ co-doped LiYF_4 nanocrystals in sol-gel derived oxyfluoride glass-ceramic. *J. Non-Cryst. Solids* **2015**, *426*, 78–82. [[CrossRef](#)]
20. Krause, W.; Nolze, G. PowderCell a program for the representation and manipulation of crystal structures and calculation of the resulting X-ray patterns. *J. Appl. Cryst.* **1996**, *29*, 301–303. [[CrossRef](#)]
21. Zaharescu, M.; Predoana, L.; Pandele, J. Relevance of thermal analysis for sol-gel-derived nanomaterials. *J. Sol-Gel Sci. Technol.* **2018**, *86*, 7–23. [[CrossRef](#)]
22. Rüssel, C. Thermal decomposition of metal trifluoroacetates. *J. Non-Cryst. Solids* **1993**, *152*, 161–166. [[CrossRef](#)]
23. PDF-ICDD. *Powder Diffraction File; PDF-4+ 2018 Software 4.18.0.2*; International Centre for Diffraction Data: Newtown Square, PA, USA, 2011.
24. Schweizer, S.; Hobbs, L.W.; Secu, M.; Spaeth, J.-M.; Edgar, A.; Williams, G.V.M. Photostimulated luminescence in Eu-doped fluorochlorozirconate glass ceramics. *Appl. Phys. Lett.* **2003**, *83*, 449. [[CrossRef](#)]
25. Wang, F.; Han, Y.; Lim, C.S.; Lu, Y.; Wang, J.; Xu, J.; Chen, H.; Zhang, C.; Hong, M.; Liu, X. Simultaneous phase and size control of upconversion nanocrystals through lanthanide doping. *Nature* **2010**, *463*, 1061–1065. [[CrossRef](#)] [[PubMed](#)]
26. Nie, L.; Shen, Y.; Zhang, X.; Wang, X.; Liu, B.; Wang, Y.; Pan, Y.; Xie, X.; Huang, L.; Huang, W. Selective Synthesis of LaF_3 and NaLaF_4 Nanocrystals via Lanthanide Ion Doping. *J. Mater. Chem. C* **2017**, *5*, 9188–9193. [[CrossRef](#)]
27. Shannon, R.D. Revised effective ionic radii and systematic studies of interatomic distances in halides and chalcogenides. *Acta Cryst. Sect. A* **1976**, *32*, 751–767. [[CrossRef](#)]
28. Chuai, X.; Liu, Z.; Liu, Y.; He, C.; Qin, W. Enhanced Near-Infrared Upconversion Luminescence of $\text{GdF}_3:\text{Yb}^{3+}, \text{Tm}^{3+}$ by Li^+ . *J. Nanosci. Nanotechnol.* **2014**, *14*, 3687–3689. [[CrossRef](#)]
29. Szpikowska-Sroka, B.; Zur, L.; Czoik, R.; Goryczka, T.; Swinarew, A.S.; Zadó, M.; Pisarski, W.A. Long-lived emission from Eu^{3+} -doped PbF_2 nanocrystals distributed into sol-gel silica glass. *J. Sol-Gel Sci. Technol.* **2013**, *68*, 278–283. [[CrossRef](#)]
30. Na, H.; Jeong, J.S.; Chang, H.J.; Kim, H.Y.; Woo, K.; Lim, K.; Mkhoyan, K.A.; Jang, H.S. Facile synthesis of intense green light emitting $\text{LiGdF}_4:\text{Yb}, \text{Er}$ -based upconversion bipyramidal nanocrystals and their polymer composite. *Nanoscale* **2014**, *6*, 7461. [[CrossRef](#)]
31. Luo, W.; Wang, Y.; Cheng, Y.; Bao, F.; Zhou, L. Crystallization and structural evolution of $\text{SiO}_2\text{-YF}_3$ xerogel. *Mater. Sci. Eng. B* **2006**, *127*, 218–223. [[CrossRef](#)]
32. Secu, C.E.; Bartha, C.; Polosan, S.; Secu, M. Thermally activated conversion of a silicate gel to an oxyfluoride glass ceramic: Optical study using Eu^{3+} probe ion. *J. Lumin.* **2014**, *146*, 539–543. [[CrossRef](#)]
33. Haase, M.; Schäfer, H. Upconverting Nanoparticles. *Angew. Chem.* **2011**, *50*, 5808–5829. [[CrossRef](#)] [[PubMed](#)]
34. Zhao, J.; Zheng, X.; Schartner, E.P.; Ionescu, P.; Zhang, R.; Nguyen, T.L.; Jin, D.; Ebdorff-Heidepriem, H. Upconversion Nanocrystal-Doped Glass: A New Paradigm for Photonic Materials. *Adv. Optical Mater.* **2016**, *4*, 1507–1517. [[CrossRef](#)]
35. Li, X.; Zhang, F.; Zhao, D. Lab on upconversion nanoparticles: Optical properties and applications engineering via designed nanostructure. *Chem. Soc. Rev.* **2015**, *44*, 1346. [[CrossRef](#)] [[PubMed](#)]
36. Chen, Y.C.; Prokleška, J.; Xu, W.J.; Liu, J.L.; Liu, J.; Zhang, W.X.; Jia, J.H.; Sechovský, V.; Tong, M. A brilliant cryogenic magnetic coolant: Magnetic and magnetocaloric study of ferromagnetically coupled GdF_3 . *J. Mater. Chem. C* **2015**, *3*, 12206–12211. [[CrossRef](#)]
37. Grzyb, T.; Mrówczyńska, L.; Szczeszak, A.; Śniadecki, Z.; Runowski, M.; Idzikowski, B.; Lis, S. Synthesis, characterization, and cytotoxicity in human erythrocytes of multifunctional, magnetic, and luminescent nanocrystalline rare earth fluorides. *J. Nanopart. Res.* **2015**, *17*, 399. [[CrossRef](#)]
38. Pauthenet, R. Spontaneous Magnetization of Some Garnet Ferrites and the Aluminum Substituted Garnet Ferrites. *J. Appl. Phys.* **1959**, *30*, 2905. [[CrossRef](#)]
39. Chen, Z.; Liu, Z.; Liu, Y.; Zheng, K.; Qin, W. Controllable synthesis, upconversion luminescence, and paramagnetic properties of $\text{NaGdF}_4:\text{Yb}^{3+}, \text{Er}^{3+}$ microrods. *J. Fluorine Chem.* **2012**, *144*, 157–164. [[CrossRef](#)]

Disclaimer/Publisher’s Note: The statements, opinions and data contained in all publications are solely those of the individual author(s) and contributor(s) and not of MDPI and/or the editor(s). MDPI and/or the editor(s) disclaim responsibility for any injury to people or property resulting from any ideas, methods, instructions or products referred to in the content.